
Generative Conformal Prediction with Vectorized Non-Conformity Scores

Minxing Zheng
University of Southern California

Shixiang Zhu
Carnegie Mellon University

Abstract

Conformal prediction (CP) provides model-agnostic uncertainty quantification with guaranteed coverage, but conventional methods often produce overly conservative uncertainty sets, especially in multi-dimensional settings. This limitation arises from simplistic non-conformity scores that rely solely on prediction error, failing to capture the prediction error distribution’s complexity. To address this, we propose a generative conformal prediction framework with vectorized non-conformity scores, leveraging a generative model to sample multiple predictions from the fitted data distribution. By computing non-conformity scores across these samples and estimating empirical quantiles at different density levels, we construct adaptive uncertainty sets using density-ranked uncertainty balls. This approach enables more precise uncertainty allocation – yielding larger prediction sets in high-confidence regions and smaller or excluded sets in low-confidence regions – enhancing both flexibility and efficiency. We establish theoretical guarantees for statistical validity and demonstrate through extensive numerical experiments that our method outperforms state-of-the-art techniques on synthetic and real-world datasets.

1 Introduction

Conformal prediction (CP) (Vovk et al., 2005) has gained prominence as a robust framework for uncertainty quantification (UQ), offering prediction sets with guaranteed coverage under minimal distributional assumptions. As a model-agnostic approach, CP can enhance any trained machine learning models to output not just point estimates but also provide uncertainty sets that contain the unobserved ground truth with user-specified high probability. As a result, CP

has found broad applications across fields such as healthcare (Seoni et al., 2023), finance (Fujimoto et al., 2022; Blasco et al., 2024), and autonomous systems (Michelmore et al., 2020; Su et al., 2023; Grewal et al., 2024), where reliable decision-making under uncertainty is critical. By delivering user-specified confidence levels, CP has become an indispensable tool for practitioners striving to connect predictive modeling with actionable, real-world insights.

While CP has proven to be a reliable and versatile framework, its prediction sets can sometimes be overly conservative (Messoudi et al., 2021), limiting their practicality and interpretability in some real-world applications. This issue often stems from the simplifying assumptions used in defining the non-conformity scores, such as the common adoption of the ℓ_2 distance. While effective in one-dimensional settings, this definition often fails to account for the complexity of multi-dimensional data distributions, especially when the data resides on a manifold (Kuleshov et al., 2018).

Several approaches have been proposed to address these limitations. For example, instead of computing the ℓ_2 distance between vectors, Neeven and Smirnov (2018) considered using elementwise distances and stacked multiple regression models to provide the uncertainty set, though it lacks theoretical validity and does not account for the dependency between variables. Other works (Messoudi et al., 2021; Sun and Yu, 2024) integrate copula function with conformal prediction to incorporate the variable dependency and provide theoretical guarantees. Yet, these methods are specifically designed for multi-target regression tasks, limiting their applicability to broader predictive tasks. More recent efforts aim to refine non-conformity scores to better capture prediction errors and adapt the prediction set to each variable. For instance, covariance-weighted non-conformity scores (Johnstone and Cox, 2021; Messoudi et al., 2022; Xu et al., 2024) provide ellipsoidal uncertainty regions that can be tailored to each data dimension. However, a fundamental limitation persists: these methods rely solely on model prediction errors and fail to leverage additional informa-

tion about the model’s predictive distribution, which could further enhance uncertainty estimation.

To address the limitations outlined above, in this paper, we introduce a novel generative conformal prediction framework with vectorized non-conformity scores to improve prediction efficiency by capturing richer distributional information. Instead of relying on a predictive model, we train a generative model to sample multiple predictions from the target distribution. Non-conformity scores are computed across these samples, and empirical quantiles are estimated at different density levels, respectively. Uncertainty sets are then constructed using adaptive-radius balls centered at the generated samples, with radii determined by the estimated quantiles. By optimally selecting quantiles across different density levels, our method produces more flexible and efficient uncertainty sets. Such density-ranked approach enables a more nuanced allocation of uncertainty: high-ranking samples from dense regions – where the model exhibits greater confidence – contribute to larger prediction sets, reflecting lower uncertainty, while lower-ranking samples from sparse regions are associated with smaller or excluded prediction sets, indicating higher uncertainty. We also establish theoretical guarantees on the statistical validity of the prediction sets. Extensive numerical studies demonstrate that our approach outperforms state-of-the-art methods on both synthetic and real-world datasets. In summary, the main contributions of this paper include:

- **GCP-VCR:** We present a novel method utilizing vectorized non-conformity scores with ranked samples to enhance the efficiency of generative CP.
- **Optimized Quantile Adjustment:** We develop an optimization framework that individually adjusts quantile levels for each rank, leading to tighter and more informative uncertainty sets.
- **Efficient Computation:** We propose an efficient heuristic algorithm to approximate the optimal quantile vector, making the method computationally practical for large datasets.
- **Theoretical and Empirical Validation:** We demonstrate through theoretical analysis and empirical evaluations that GCP-VCR maintains valid coverage while significantly improving prediction set efficiency compared to baseline methods.

Related Work Other than conformal prediction, there have been several approaches proposed to quantify uncertainty such as Bayesian based methods (Blundell et al., 2015; Krueger et al., 2017; Mobiny et al., 2021), and ensemble based methods (Lakshminarayanan et al., 2017; Valdenegro-Toro, 2019; McDermott and Wikle, 2019; Wen et al., 2020). We refer to several survey papers (Gawlikowski et al., 2023; Abdar

et al., 2021; He and Jiang, 2023) for further details of works in these uncertainty quantification methods.

In terms of conformal prediction, extended works have been done focusing on CP for deterministic models. Different summary statistics of the conditional distribution have been studied, for example, mean (Shafer and Vovk, 2008; Lei et al., 2018) and quantiles (Romano et al., 2019; Kivaranovic et al., 2020; Alaa et al., 2023). In Sesia and Romano (2021), the authors use histograms to estimate the conditional distribution and provide efficient prediction intervals with approximate conditional coverage. Though the above methods all provide continuous prediction intervals, they cannot adapt to multimodality well. In Lei et al. (2013) and Lei and Wasserman (2014), the authors first consider the aspect of density level sets and density-based clustering for providing efficient prediction set. The authors use kernel density estimator to construct the non-conformity scores and with a proper choice of bandwidth, the prediction set could be discontinuous. There are also following works (Izbicki et al., 2019; Chernozhukov et al., 2021; Izbicki et al., 2022) that estimate the density or cumulative distribution function to construct prediction sets. As a reminder, in our setting, we only need access to the random samples generated from the fitted model instead of explicit density estimation. So our setting is more generic and applicable to real applications. Other than density estimation, (Tumu et al., 2024) fits shape functions (convex hull, hyperrectangle, and ellipsoid) on the calibration data to provide a discontinuous prediction set as a union of fitted shapes. In Guha et al. (2024), the authors convert regression to a classification problem and can provide discontinuous prediction sets with interpolation of classification scores.

Efficiency, measured by the size of the prediction set, is a fundamental assessment of the quality of a CP method. Some works explore the effect of different non-conformity score measures such as by scaling and reweighting the non-conformity score of each calibration data (Papadopoulos et al., 2002, 2011; Kivaranovic et al., 2020; Bellotti, 2020; Amoukou and Brunel, 2023). On the other hand, some works (Stutz et al., 2021; Einbinder et al., 2022) directly reduce inefficiency by incorporating a differentiable inefficiency measurement into the training loss. Bai et al. (2022) reformulate CP as a constrained optimization problem. By introducing an extra parameter and enriching the search space of the optimization problem, it demonstrates better performance in efficiency. Our main idea is partially motivated by this reformulation. We also gain insights from the recent development of CP for multi-target regression tasks and the definition of multivariate quantile function as discussed in (Messoudi

et al., 2021; Sun and Yu, 2024).

Recent advancements, such as probabilistic conformal prediction (PCP) using conditional random samples (Wang et al., 2023), have paved the way for CP in probabilistic and generative models. PCP leverages generated random samples to construct the prediction sets in the form of a union of balls around each generated sample, offering a discontinuous uncertainty set. This is a fundamental step towards better coverage efficiency, as ideally, we want the prediction set to avoid low-density regions. However, PCP faces two major limitations: i) PCP does not distinguish different generated samples and assigns the same radius to each ball, ii) when the number of generated samples is relatively small, PCP can yield overly conservative prediction sets. We will discuss the comparison of our proposed method and PCP in details in section 3.3.

2 Preliminaries

Conformal Prediction (CP) is a general framework for uncertainty quantification that produces statistically valid prediction regions for any underlying point predictor, only assuming exchangeability of the data (Angelopoulos et al., 2023). Consider a dataset of n data pairs: $\mathcal{D} = \{(X_i, Y_i)\}_{i=1}^n$, where $X_i \in \mathcal{X} \subseteq \mathbb{R}^q$ are the features and $Y_i \in \mathcal{Y} \subseteq \mathbb{R}^d$ are the responses. Given a new test pair (X_{n+1}, Y_{n+1}) , which is assumed to be exchangeable with the observations in \mathcal{D} , the goal of CP is to construct a prediction set $\hat{\mathcal{C}}(X_{n+1})$ based on the calibration data \mathcal{D} such that, for a user-defined miscoverage rate α , the following condition holds:

$$\mathbb{P}(Y_{n+1} \in \hat{\mathcal{C}}(X_{n+1})) \geq 1 - \alpha. \quad (1)$$

This ensures that the prediction set $\hat{\mathcal{C}}(\cdot)$ covers the true label with a probability of at least $1 - \alpha$, where the probability is marginal over the calibration data and the test point.

To achieve this, CP computes a non-conformity score, which measures the extent to which a new data point conforms to the behavior of the training data under a predictive model. For regression tasks, a typical choice of non-conformity score is the absolute residuals from a predictive model \hat{f} , *i.e.*, $E_i = |Y_i - \hat{f}(X_i)|$. Based on this score, the empirical quantile of the non-conformity scores of calibration data is calculated to construct prediction set $\hat{\mathcal{C}}(X_{n+1})$ such that the miscoverage rate condition (1) is satisfied.

Prediction Set Efficiency. Beyond ensuring valid coverage, *efficiency* is a key evaluation metric of CP’s performance, assessed by the size of the prediction set $|\hat{\mathcal{C}}(X_{n+1})|$. While a trivial prediction set that includes the entire response space would guarantee coverage, it offers little practical value for decision-making. There-

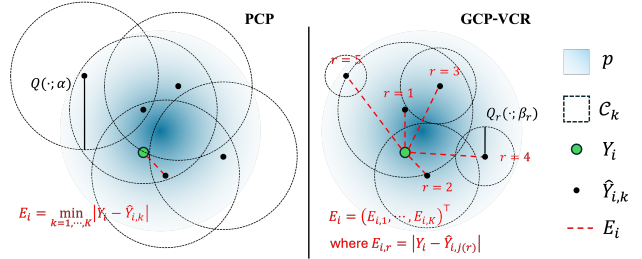


Figure 1: An illustrative comparison between the proposed GCP-VCR and PCP, where GCP-VCR provides a more flexible and efficient prediction set. The non-conformity score vector $(E_{i,1}, \dots, E_{i,K})^\top$ provides more detailed information on the underlying distribution represented by the blue area. Samples in denser regions (darker blue) are ranked higher (small r), indicating greater model confidence and larger \mathcal{C}_r sizes, while low-rank scores (large r) capture uncertainty in sparser regions, where \mathcal{C}_r sizes are smaller.

fore, we aim to produce prediction sets that are as informative (*i.e.*, small) as possible while maintaining the coverage guarantee.

3 Proposed Method

In this section, we introduce a novel method, referred to as Generative Conformal Prediction with Vectorized Non-Conformity Scores (GCP-VCR), which utilizes a vectorized non-conformity score with ranked samples.

Generative models offer a versatile framework for capturing complex data distributions, advancing beyond deterministic models that output limited summary statistics (e.g., mean or quantiles). Let $\hat{p}(Y|X)$ denote a fitted generative model from which conditional random samples can be drawn, e.g., $\hat{Y}_1, \dots, \hat{Y}_K \sim \hat{p}(Y|X)$. These random samples encode nuanced information of the prediction error distribution—such as multimodal patterns and tail behaviors—that traditional scalar non-conformity scores fail to capture. Leveraging this information enables more robust and efficient uncertainty quantification. To fully exploit this information, we propose a vectorized non-conformity score that aggregates prediction errors across all generated samples. We further rank these samples by their empirical density, prioritizing high-density regions where the model is confident and assigning adaptive quantile levels to samples at different ranks. This ranking mechanism enables localized uncertainty allocation by distinguishing high-confidence and low-confidence samples. We formalize this process as a constrained optimization problem to derive the optimal quantile vector, ensuring both statistical validity and uncertainty set efficiency. Figure 1 highlights our advancements compared to PCP, while Algorithm 1 outlines the complete workflow. The following sections detail

Algorithm 1 GCP-VCR

1: **Input:** Conditional probabilistic model $\hat{p}(Y|X)$;
calibration data \mathcal{D} ; testing feature X_{n+1} ; coverage
rate $1 - \alpha$; number of random samples K .
2: // Calibration
3: Initialize $\mathcal{E} \leftarrow \emptyset$;
4: **for** $(X_i, Y_i) \in \mathcal{D}$ **do**
5: Sample $\{\hat{Y}_{i,k}\}_{k=1}^K \sim \hat{p}(Y|X_i)$;
6: $\{\hat{Y}_{i,j(r)}\}_{r=1}^K \leftarrow \text{Rank } \{\hat{Y}_{i,k}\}_{k=1}^K$ by (2);
7: $E_i \leftarrow \text{Compute (3) for each } r$;
8: $\mathcal{E} \leftarrow \mathcal{E} \cup E_i$;
9: **end for**
10: $\beta^* \leftarrow \text{argmin of (6) calculated with } \mathcal{E}$;
11: // Testing
12: Sample $\{\hat{Y}_{n+1,k}\}_{k=1}^K \sim \hat{p}(Y|X_{n+1})$;
13: $\{\hat{Y}_{n+1,j(r)}\}_{r=1}^K \leftarrow \text{Rank } \{\hat{Y}_{n+1,k}\}_{k=1}^K$ by (2);
14: **Output:** $\hat{\mathcal{C}}_{\text{VCR}}(X_{n+1}; \beta^*)$ in (4).

our method step by step rigorously.

3.1 Vectorized Non-Conformity Score

For each calibration data (X_i, Y_i) , its vectorized non-conformity score can be constructed as follows:

1. Generate K samples $\{\hat{Y}_{i,k}\}_{k=1}^K$ from $\hat{p}(\cdot|X_i)$.
2. Rank these K samples based on their average m -nearest neighbor distances, denoted by $\{\bar{D}_{i,k}\}_{k=1}^K$, where $\bar{D}_{i,k}$ represents the average distance from $\hat{Y}_{i,k}$ to its m nearest neighbors among the generated samples:

$$\bar{D}_{i,j(1)} \leq \dots \leq \bar{D}_{i,j(K)}, \quad (2)$$

where $j(r)$ denotes the index of the r -th sorted sample. Detailed computation of the average m -nearest neighbor distances can be found in Appendix A.

3. The non-conformity score vector can be obtained by

$$(E_{i,1}, \dots, E_{i,K})^\top \in \mathbb{R}^K,$$

where each $E_{i,r}$ is the distance between label Y_i and the r -th sorted sample $\hat{Y}_{i,j(r)}$, defined as

$$E_{i,r} = \|Y_i - \hat{Y}_{i,j(r)}\|. \quad (3)$$

The rationale of constructing the non-conformity score vector with ranked samples is two-fold: (i) By forming a vector of non-conformity scores rather than a single scalar value, we capture more detailed information about the relationship between the true label Y_i and the generated samples. Each element $E_{i,r}$ in the vector corresponds to a specific rank r , reflecting different aspects of the sample distribution. This enriched information enables us to construct more flexible and informative prediction sets compared to traditional CP methods that rely on a scalar score. (ii)

Ranking the samples based on their average m -nearest neighbor distances allows us to identify and prioritize samples located in denser regions of the estimated model \hat{p} . Samples with smaller $\bar{D}_{i,j(1)}$ are presumed to be in high-density areas and are thus ranked higher. Consequently, the non-conformity scores $E_{i,r}$ for different ranks r carry varying significance: High-rank scores (r is small) correspond to samples in denser regions, where the model is more confident, whereas low-rank scores (r is large) represent samples in sparser regions, capturing the model's uncertainty. By comparing non-conformity scores across different calibration data points at the same rank, we can assess discrepancies at multiple levels of the distribution. This stratified approach provides a more nuanced understanding of the model's performance across the entire output space, leading to more accurate and adaptive uncertainty sets.

We note that the choice of distance measure in (3) can be adapted based on the nature of \mathcal{Y} . For instance, if \mathcal{Y} resides in Euclidean space, the ℓ_p norm may be adopted. In the context of geographical data, the distance measure could be the geodesic distance or even a general kernel function, depending on the application.

3.2 Efficiency-Enhanced Prediction Set

The prediction set can be constructed as follows: First, we compute the non-conformity score vectors $\{E_i := (E_{i,1}, \dots, E_{i,K})^\top\}_{i=1}^n$ for the calibration data \mathcal{D} . Then, for a new test pair (X_{n+1}, Y_{n+1}) , we define the prediction set as follows:

$$\hat{\mathcal{C}}_{\text{VCR}}(X_{n+1}; \beta) = \cup_{r=1}^K \hat{\mathcal{C}}_r(\beta_r), \quad (4)$$

where $\beta := \{\beta_r\}_{r=1}^K$ and each $\hat{\mathcal{C}}_r(\beta_r)$ is defined by

$$\hat{\mathcal{C}}_r(\beta_r) = \left\{ y : \|y - \hat{Y}_{n+1,j(r)}\| \leq Q_r(\{E_{1,r}, \dots, E_{n,r}\} \cup \{\infty\}; \beta_r) \right\},$$

and $Q_r(\cdot; \beta_r)$ is the $(1 - \beta_r)$ -th quantile function. For notational simplicity, we use $Q_r(\beta_r) = Q_r(\{E_{1,r}, \dots, E_{n,r}\} \cup \{\infty\}; \beta_r)$ throughout the paper.

If the distance measure in (3) is the ℓ_2 -norm, the resulting prediction set becomes a union of balls centered at each generated sample $\hat{Y}_{n+1,j(r)}$, with rank-dependent radius determined by $Q_r(\beta_r)$. Introducing the quantile vector $(Q_r(\beta_1), \dots, Q_r(\beta_K))^\top$ allows each rank r to have its own quantile level β_r , offering greater flexibility in constructing prediction sets. This approach enables us to optimize the quantiles individually for each rank, leading to more efficient and tighter uncertainty sets while still ensuring valid coverage – even though the β_r values are not necessarily equal to the user-defined miscoverage rate α . As a comparison,

PCP provides the uncertainty set as a union of equal-sized balls; a detailed comparison with PCP will be presented in Section 3.3.

Quantile Optimization We aim to find optimal quantile vector $\beta = (\beta_1, \dots, \beta_K)^\top$ that maximize the predictive efficiency (*i.e.*, minimize the size of the prediction set) while ensuring the coverage validity.

To assess efficiency, we consider the total volume of all balls, which serves as an upper bound on the true size of the prediction set for computational simplicity:

$$\sum_{r=1}^K (Q_r(\beta_r))^d \propto \sum_{r=1}^K \hat{C}_r(\beta_r) \geq |\hat{C}_{\text{VCR}}(\beta)|,$$

where d is the dimensionality of the response variable Y . The calibration coverage rate is defined as

$$\frac{1}{n+1} \sum_{i=\{1, \dots, n, \infty\}} \hat{S}_i(\beta), \quad (5)$$

where we let $E_{\infty, r} = \infty$ for any r , and define

$$\hat{S}_i(\beta) := \max_{r=1, \dots, K} \mathbb{1}\{E_{i, r} \leq Q_r(\beta_r)\}.$$

Intuitively, each $\hat{S}_i(\beta)$ equals 1 if there is at least one ball in the prediction set covers the calibration data Y_i . Here, the denominator $n+1$ and use of $\hat{S}_\infty(\beta)$ is for theoretical proof of coverage validity, and can be understood as a finite-sample correction. Formally, given the non-conformity score vectors, we formulate the following optimization problem:

$$\begin{aligned} & \min_{\beta} \left\{ \sum_{r=1}^K (Q_r(\beta_r))^d \right\}, \\ \text{s.t. } & \frac{1}{n+1} \sum_{i=\{1, \dots, n, \infty\}} \hat{S}_i(\beta) \geq 1 - \alpha. \end{aligned} \quad (6)$$

We denote the optimal solution of this optimization problem as β^* . In the following theorem, we demonstrate that the prediction set $\hat{C}_{\text{VCR}}(X_{n+1}; \beta^*)$ provides valid coverage:

Theorem 3.1 (Validity of GCP-VCR). *For testing data (X_{n+1}, Y_{n+1}) that is exchangeable with calibration \mathcal{D} , the prediction set $\hat{C}_{\text{VCR}}(X_{n+1}; \beta^*)$ provides valid coverage, *i.e.*,*

$$\mathbb{P}(Y_{n+1} \in \hat{C}_{\text{VCR}}(X_{n+1}; \beta^*)) \geq 1 - \alpha.$$

The proof of Theorem 3.1 is presented in Appendix B.

Remark 3.2. We note that the proof of Theorem 3.1 is non-trivial, as it involves handling non-conformity score vectors. For scalar non-conformity scores, the

quantile is unique and can be readily determined by sorting the scalar values. However, with multivariate vectors, two primary challenges arise in computing the quantile: (*i*) The quantile is represented by a vector, in which its value is not unique (*ii*) There is no (total) ordering between vectors, meaning that vectors are not fully comparable and thus cannot be sorted as scalars are. To overcome these challenges, we define a partial ordering between vectors and select the vector that maximizes efficiency while ensuring validity.

Efficient Algorithm for Quantile Optimization. Solving problem (6) becomes computationally infeasible for larger values of K (*e.g.*, $K \geq 5$) due to the exponential growth of the search space. To tackle this challenge, we introduce an iterative algorithm that approximates the optimal quantile vector in linear time by simplifying the search process. The key idea is to activate one quantile at a time while setting others to default values, and then perform pairwise trade-offs between quantiles of different ranks to enhance efficiency. Specifically, we initialize the algorithm by setting $\beta_r = 0$ for a selected rank r , with all other $\beta_s = 1$ for $s \neq r$, reducing the non-conformity score vector to a scalar case. We incrementally increase β_r by a small step size ϵ until the empirical coverage just exceeds the target level $1 - \alpha$. Subsequently, we iteratively adjust β_r and other β_s by trading off small increments and decrements while maintaining the coverage constraint, accepting adjustments that improve efficiency. This process has a computational complexity of $\mathcal{O}(Kn)$ (or $\mathcal{O}(K^2n)$ when iterating over all positions) and empirically yields an approximate solution $\hat{\beta}$ that achieves superior efficiency compared to baseline methods. A demonstration of the coverage efficiency across iterations and the solution path of the approximated solution with different initializations is presented in Figure 2. The details of the algorithm can be found in Algorithm 2 in Appendix C.

Corollary 3.3 (Validity of Approximated Solution). *For any approximated solution $\hat{\beta}$ output by Algorithm 2 and testing data (X_{n+1}, Y_{n+1}) that is exchangeable with calibration \mathcal{D} , the prediction set $\hat{C}_{\text{VCR}}(X_{n+1}; \hat{\beta})$ provides valid coverage, *i.e.*,*

$$\mathbb{P}(Y_{n+1} \in \hat{C}_{\text{VCR}}(X_{n+1}; \hat{\beta})) \geq 1 - \alpha.$$

The proof of Theorem 3.3 is presented in Appendix B

3.3 Comparison with PCP

Probabilistic Conformal Prediction (PCP) (Wang et al., 2023) first studied CP for generative models and utilized the information of random samples. In contrast to our method, which considers all the distances between each random sample and the true response, PCP defines its non-conformity score as the

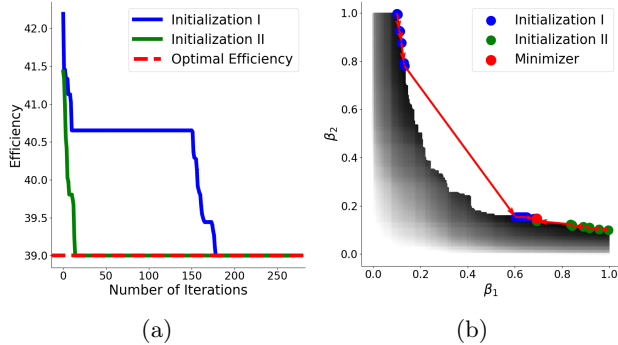


Figure 2: Demonstration of the proposed approximated algorithm. Subplot 2a presents the efficiency of approximated solutions with different initializations toward optimal efficiency over iterations. Subplot 2b presents the solution paths of the approximated solutions for different initialization, with arrows indicating the path direction over iterations. The shaded area is the feasible region of the optimization problem, and the darker regions correspond to higher efficiency.

minimum distance between random samples and the true response:

$$E_i = \min_{k=1, \dots, K} \|Y_i - \hat{Y}_{i,k}\|. \quad (7)$$

for each calibration data (X_i, Y_i) . For a new test data (X_{n+1}, Y_{n+1}) , the prediction set of PCP is constructed as the union of K regions:

$$\hat{C}(X_{n+1}) = \cup_{k=1}^K \hat{C}_k, \quad (8)$$

where each region \hat{C}_k is defined by

$$\hat{C}_k = \left\{ y : \|y - \hat{Y}_{n+1,k}\| \leq Q(E_{1:n} \cup \{\infty\}; \alpha) \right\}.$$

Here $Q(\cdot; \alpha)$ is the $1 - \alpha$ quantile of the empirical distribution of the non-conformity scores E_1, \dots, E_n .

As noted, PCP adopts a scalar non-conformity score, which assigns a uniform radius to all prediction regions \hat{C}_k . This uniform treatment of random samples limits adaptability, as ideally, high-density regions should have larger radius, while low-density regions require smaller ones. In contrast, GCP-VCR introduces a vectorized non-conformity score that captures the full complexity of the prediction error distribution. By ranking samples based on their empirical density, our method enables individualized optimization of the ball radius for each sample. As demonstrated in Figure 4, the ball radius for low-density regions nearly diminishes, highlighting the flexibility of our approach. Another limitation of PCP arises when K is small. In such cases, the empirical distribution of minimum distances may become heavy-tailed, requiring a large quantile (radius) to maintain coverage, leading to a conservative prediction set $\hat{C}(X_{n+1})$. In contrast, GCP-VCR overcomes this by introducing

an individualized quantile selection, relaxing the constraint for attaining the $1 - \alpha$ quantile uniformly across all samples at each rank and reducing the impact of the distribution’s tail. As shown in Figure 2b, where the target $\alpha = 0.1$, but neither β_1 nor β_2 needs to be smaller than α to achieve the optimal efficiency.

4 Experiments

In this section, we evaluate the empirical performance of GCP-VCR compared with several state-of-the-art baselines on five synthetic data, one semi-synthetic data, and four real-world datasets. We demonstrate the superior efficiency and coverage validity of GCP-VCR, especially in handling multimodal and heterogeneous distributions.

Baselines: We consider the following five baseline methods: (i) conformalized quantile regression (CQR) (Romano et al., 2019), (ii) conformal histogram regression (CHR) (Sesia and Romano, 2021), (iii) probabilistic conformal prediction (PCP) (Wang et al., 2023), (iv) regression-to-classification conformal prediction (R2CCP) (Guha et al., 2024), and (v) conformal region designer (CRD) (Tumu et al., 2024). CQR and CHR estimate conditional quantiles and conditional histograms, respectively, to construct the prediction set. R2CCP converts regression to a classification problem and interpolates the classification scores to construct the non-conformity score for the regression problem. CRD fits shapes (hyperrectangle, ellipsoid, and convex hull) and optimizes their total volume to construct prediction sets. Among the baseline methods, CQR and CHR only produce continuous prediction sets, whereas all the other methods can provide discontinuous prediction sets. For the conditional quantile and histogram estimation of CQR and CHR, we apply the quantile regression neural network model (Taylor, 2000) and quantile regression forest (Meinshausen, 2006). The implementation of each baseline method is based on their public GitHub.

Implementation Configuration: In all the following experiments, we consider the miscoverage rate $\alpha = 0.1$ and evaluate the results based on the empirical coverage rate (Cover) and prediction set efficiency (Eff). The choice of hyperparameter K is a trade-off between coverage efficiency and computational cost. Intuitively, with more random samples, samples can be ranked more accurately and better reflect the estimated conditional distribution, thus outputting more efficient prediction set. However, it also incurs with higher computational costs. In our experiments, we set $K = 10, 20, 50$ for different datasets, with the specifics elaborated in the following section. In comparison, Wang et al. (2023) choose $K = 1,000$ for real

Table 1: Summary of synthetic data results.

Dataset	Metric ¹	CQR	CHR	CRD	R2CCP	PCP	GCP-VCR
S-shape	Cover	0.90 ± 0.02	0.90 ± 0.02	0.89 ± 0.09	0.90 ± 0.02	0.90 ± 0.02	0.89 ± 0.02
	Eff	3.41 ± 0.07	3.43 ± 0.08	6.98 ± 0.79	3.05 ± 0.20	0.59 ± 0.11	0.55 ± 0.08
Mix-Gaussian	Cover	0.90 ± 0.02	0.91 ± 0.02	0.93 ± 0.03	0.90 ± 0.02	0.90 ± 0.01	0.88 ± 0.01
	Eff	30.5 ± 0.00	31.01 ± 1.63	92.17 ± 8.8	35.09 ± 1.79	19.49 ± 2.44	18.43 ± 2.46
Spirals	Cover	0.90 ± 0.01	0.90 ± 0.01	0.90 ± 0.03	0.89 ± 0.00	0.90 ± 0.01	0.89 ± 0.01
	Eff	20.20 ± 0.71	19.47 ± 0.61	44.48 ± 2.98	12.84 ± 0.31	3.39 ± 0.21	3.19 ± 0.18
Circles	Cover	0.90 ± 0.02	0.90 ± 0.02	0.90 ± 0.02	0.89 ± 0.00	0.90 ± 0.02	0.88 ± 0.02
	Eff	1.72 ± 0.03	1.46 ± 0.11	2.91 ± 0.43	1.02 ± 0.01	0.88 ± 0.05	0.85 ± 0.05
Unbalanced Cluster	Cover	0.90 ± 0.02	0.90 ± 0.02	0.90 ± 0.03	0.90 ± 0.02	0.90 ± 0.02	0.88 ± 0.02
	Eff	12.29 ± 0.17	12.04 ± 0.20	15.34 ± 1.58	12.83 ± 0.95	6.98 ± 0.64	6.79 ± 0.67

¹ We evaluate the performance for each method with empirical coverage rate (Cover) and prediction set efficiency (Eff). Each cell contains the averaged metric value along with the standard error over 100 independent experiments.

data analysis. We also aim to provide results of the method’s performance when the choice of K is limited. We take $m = \lceil K/3 \rceil$ for the m -nearest neighbor distance calculation. To generate conditional random samples, we implement the conditional nearest neighbor density estimation method in Izbicki and B. Lee (2017) for 1-dimensional synthetic data and the mixture density network (Bishop, 1994; Rothfuss et al., 2019) for the other datasets as the base models. Further details of the implementation of each method, synthetic data generation, and modeling procedure can be found in Appendix D.

4.1 Synthetic Data

We evaluate the methods on five synthetic datasets: S-shape, Spirals, Circles, Unbalanced cluster for $Y \in \mathbb{R}$ and Mix-Gaussian for $Y \in \mathbb{R}^2$. The conditional distribution of all the datasets presents multimodality and some are also heterogeneous. We set $K = 20$ for Mix-Gaussian data and $K = 10$ for the other four data. Each data contains 5,000 random observations and we split the data into 60/20/20 for training, calibration, and testing separately.

We present the summary of the synthetic data results averaged over 100 experiments in Table 1 and highlight the most efficient method for each data. Overall, all methods achieve valid coverage rates, while GCP-VCR produces the most efficient prediction set. The visualizations of the prediction sets of different methods on these data are presented in Appendix E.1. We can observe that PCP and GCP-VCR can consistently provide discontinuous prediction sets and, thus are much more efficient than other methods for multimodal settings. Compared with PCP, GCP-VCR provides a more flexible and locally-adaptive prediction set, *i.e.*, the coverage region of GCP-VCR is larger in the high-density region and smaller in the low-density region, especially in the Mix-Gaussian setting. This is the benefit that vectorized non-conformity scores provide

compared with a scalar.

4.2 MNIST: Digit Image Generation

We design a semi-synthetic experiment with the MNIST image dataset (Deng, 2012) to assess the applicability and interpretability of GCP-VCR to high-dimensional data. Conformal prediction in high-dimensional data, such as images, texts, and audio, presents a unique challenge for interpreting prediction sets, as it is inapplicable to iterate over the entire space of target variables.

Consider the setting that given $X \in \{0, \dots, 9\}$, the corresponding Y is an image of digit X . We train a variational-autoencoder (VAE) and create the prediction set in the latent embedding space. For the conditional sampling process, we assume access to an independent sampler that generates random images of digit X not presented in the training/calibration/testing process. We then embed the sampled images with the trained encoder and construct the prediction set in the embedding space. Ahead of training, we will split part of the dataset for the sampler so that it is independent of the following process. The reason that we design this sampler instead of training a conditional VAE (cVAE) is that the embedding space of VAE tends to be more clustered than cVAE, thus the prediction set can be better demonstrated for illustrative purposes.

Figure 3 shows samples from the prediction set provided by PCP and GCP-VCR with $K = 40$ conditioning on different X values in each row. For each X , we randomly sample 9 images from the prediction set of PCP and GCP-VCR. Both of the methods achieve valid coverage rates. We can observe that the sampled images of GCP-VCR align closer with the target image for each X , indicating a tighter and more efficient prediction set of GCP-VCR. Quantitatively, as it is not applicable to directly measure the size of the prediction set, we propose to evaluate the miscover-

Table 2: Summary of real data results.

Dataset	Metric	CQR	CHR	CRD	R2CCP	PCP	GCP-VCR
Fb1	Cover	0.97 ± 0.00	0.90 ± 0.02	0.85 ± 0.16	0.33 ± 0.00	0.93 ± 0.01	0.89 ± 0.02
	Eff	19.78 ± 1.95	9.50 ± 0.81	58.31 ± 62.27	7.96 ± 0.00	9.05 ± 9.01	4.84 ± 2.38
Fb2	Cover	0.97 ± 0.01	0.90 ± 0.01	0.90 ± 0.02	0.52 ± 0.25	0.93 ± 0.01	0.89 ± 0.01
	Eff	19.34 ± 1.43	9.52 ± 0.90	44.16 ± 33.98	11.04 ± 2.00	8.48 ± 8.83	4.35 ± 1.90
Blog	Cover	0.97 ± 0.01	0.90 ± 0.01	0.89 ± 0.01	0.32 ± 0.58	0.92 ± 0.02	0.90 ± 0.01
	Eff	22.01 ± 2.01	9.71 ± 1.21	24.56 ± 8.45	11.04 ± 2.00	11.04 ± 2.50	3.96 ± 2.23
Bike	Cover	0.91 ± 0.01	0.90 ± 0.01	0.90 ± 0.01	0.90 ± 0.02	0.90 ± 0.01	0.89 ± 0.01
	Eff (10^{-3})	1510 ± 10	4.7 ± 0.10	10.71 ± 3.78	0.79 ± 0.09	0.73 ± 0.26	0.57 ± 0.06

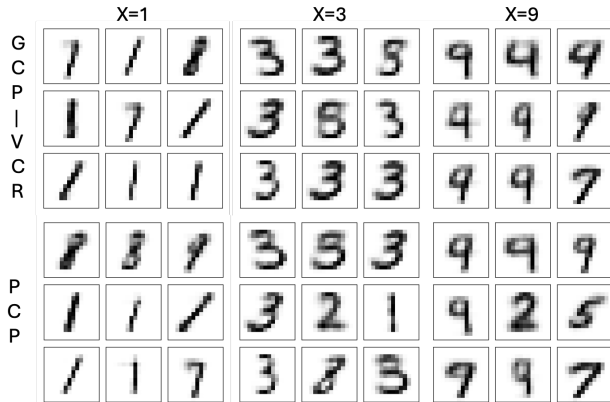


Figure 3: Comparison of MNIST images sampled from prediction sets of GCP-VCR and PCP, respectively. Each column corresponds to different values of X . The randomly sampled images of GCP-VCR align more closely with the target X compared to PCP, indicating tighter prediction sets with fewer incorrect images.

age rate. It measures the empirical probability of an incorrect image falling into the prediction set. Under $K = 40$, GCP-VCR attains an average miscoverage rate of 0.16 ± 0.02 (standard error) over 30 experiments, compared to 0.22 ± 0.03 for PCP. In Appendix E.2, we also present the comparison of the miscoverage rate of PCP and GCP-VCR under different choices of K . It shows that GCP-VCR consistently attains a lower miscoverage rate than PCP.

4.3 Real Data

We apply GCP-VCR along with baseline methods on four real-world datasets: blog feedback (Blog) Buza (2014), facebook comment volume Singh (2015) variant 1 (Fb1) and variant 2 (Fb2), and New York City bike sharing (Bike). For each dataset, we randomly sample 30,000 samples for training, 1,000 samples for calibration and 1,000 for testing. We set $K = 50$ for the Bike dataset, and $K = 20$ for the rest datasets. The summary of the real data results averaging over 30 experiments is presented in Table 2. Overall, GCP-VCR achieves the highest efficiency while maintaining the coverage rate. Notably, the efficiency gains of

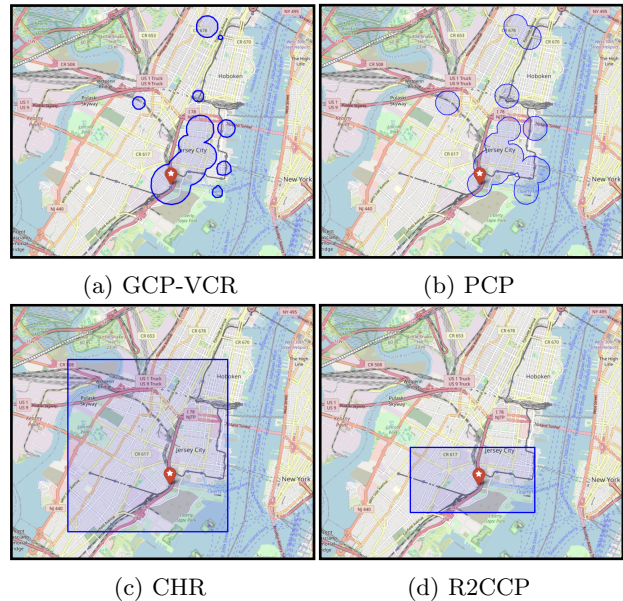


Figure 4: Comparison of prediction sets across four methods that have the highest efficiency on Bike dataset. The colored area indicates the prediction set, and the red marker is the target location.

GCP-VCR are more pronounced on real datasets compared to synthetic data, which we attribute to such a difference in data complexity. Real datasets, such as the blog dataset with 280 features, exhibit highly complex conditional distributions $Y|X$, highlighting GCP-VCR’s efficiency and robustness in handling intricate data structures. In contrast, synthetic data with only a single feature, inherently has lower distributional complexity, leaving limited room for improvement. Additionally, we observe that for the first three datasets, R2CCP suffers from undercoverage issues and exhibits high variance in coverage rates across experiments.

We present a visual demonstration of the prediction set generated by our method, PCP, CHR and R2CCP in Figure 4, respectively. The blue region indicates the prediction set by each method and the red star marker indicates the target location. Both PCP and our method can deliver discontinuous coverage regions, whereas CHR and R2CCP provide a rectangle-shaped

continuous set. It is also noted that, compared with PCP, GCP-VCR assigns larger circles' radius to high-density regions while nearly vanishing the circles' radius in low-density regions. Specifically, the circle at the top of the map lies in a low-density region, it almost shrinks to a point and disappears for GCP-VCR, whereas it remains large for PCP. Thus, GCP-VCR leads to significant improvements in flexibility and efficiency of prediction set.

5 Discussion and Conclusion

We introduced GCP-VCR, a novel conformal prediction method for generative models that leverages vectorized non-conformity scores with ranked samples to improve prediction set efficiency. By ranking conditional samples, our method captures nuanced error distribution and explores structural relationships among samples. Optimizing each entry of the non-conformity score vector separately enables a more flexible and data-adaptive prediction set. Specifically, GCP-VCR constructs discontinuous prediction sets as a union of regions centered at random samples, where the radius of each region is adapted to the model's uncertainty level of each sample. We also proposed a computationally efficient algorithm to approximate the optimal quantile vector, ensuring scalability to large datasets.

Through extensive experiments on both synthetic and real-world datasets, GCP-VCR consistently demonstrated superior efficiency while maintaining coverage validity. In the MNIST experiment, we showcased the potential power of GCP-VCR in high-dimensional data, illustrating its ability to improve the reliability of predictions in modern high-stakes applications.

References

- Abdar, M., Pourpanah, F., Hussain, S., Rezazadegan, D., Liu, L., Ghavamzadeh, M., Fieguth, P., Cao, X., Khosravi, A., Acharya, U. R., et al. (2021). A review of uncertainty quantification in deep learning: Techniques, applications and challenges. *Information fusion*, 76:243–297.
- Alaa, A. M., Hussain, Z., and Sontag, D. (2023). Conformalized unconditional quantile regression. In Ruiz, F., Dy, J., and van de Meent, J.-W., editors, *Proceedings of The 26th International Conference on Artificial Intelligence and Statistics*, volume 206 of *Proceedings of Machine Learning Research*, pages 10690–10702. PMLR.
- Amoukou, S. I. and Brunel, N. J. (2023). Adaptive conformal prediction by reweighting nonconformity score. *arXiv preprint arXiv:2303.12695*.
- Angelopoulos, A. N., Bates, S., et al. (2023). Conformal prediction: A gentle introduction. *Foundations and Trends® in Machine Learning*, 16(4):494–591.
- Bai, Y., Mei, S., Wang, H., Zhou, Y., and Xiong, C. (2022). Efficient and differentiable conformal prediction with general function classes. *arXiv preprint arXiv:2202.11091*.
- Bellotti, A. (2020). Constructing normalized nonconformity measures based on maximizing predictive efficiency. In Gammerman, A., Vovk, V., Luo, Z., Smirnov, E., and Cherubin, G., editors, *Proceedings of the Ninth Symposium on Conformal and Probabilistic Prediction and Applications*, volume 128 of *Proceedings of Machine Learning Research*, pages 41–54. PMLR.
- Bishop, C. M. (1994). Mixture density networks.
- Blasco, T., Sánchez, J. S., and García, V. (2024). A survey on uncertainty quantification in deep learning for financial time series prediction. *Neurocomputing*, 576:127339.
- Blundell, C., Cornebise, J., Kavukcuoglu, K., and Wierstra, D. (2015). Weight uncertainty in neural network. In *International conference on machine learning*, pages 1613–1622. PMLR.
- Buza, K. (2014). BlogFeedback. UCI Machine Learning Repository. DOI: <https://doi.org/10.24432/C58S3F>.
- Chernozhukov, V., Wüthrich, K., and Zhu, Y. (2021). Distributional conformal prediction. *Proceedings of the National Academy of Sciences*, 118(48):e2107794118.
- Deng, L. (2012). The mnist database of handwritten digit images for machine learning research. *IEEE Signal Processing Magazine*, 29(6):141–142.
- Einbinder, B.-S., Romano, Y., Sesia, M., and Zhou, Y. (2022). Training uncertainty-aware classifiers with conformalized deep learning. In Oh, A. H., Agarwal, A., Belgrave, D., and Cho, K., editors, *Advances in Neural Information Processing Systems*.
- Fujimoto, Y., Nakagawa, K., Imajo, K., and Minami, K. (2022). Uncertainty aware trader-company method: Interpretable stock price prediction capturing uncertainty. In *2022 IEEE International Conference on Big Data (Big Data)*, pages 1238–1245.
- Gawlikowski, J., Tassi, C. R. N., Ali, M., Lee, J., Humt, M., Feng, J., Kruspe, A., Triebel, R., Jung, P., Roscher, R., et al. (2023). A survey of uncertainty in deep neural networks. *Artificial Intelligence Review*, 56(Suppl 1):1513–1589.
- Grewal, R., Tonella, P., and Stocco, A. (2024). Predicting safety misbehaviours in autonomous driving systems using uncertainty quantification. *arXiv preprint arXiv:2404.18573*.

- Guha, E. K., Natarajan, S., Möllenhoff, T., Khan, M. E., and Ndiaye, E. (2024). Conformal prediction via regression-as-classification. In *The Twelfth International Conference on Learning Representations*.
- He, W. and Jiang, Z. (2023). A survey on uncertainty quantification methods for deep neural networks: An uncertainty source perspective. *arXiv preprint arXiv:2302.13425*.
- Izbicki, R. and B. Lee, A. (2017). Converting high-dimensional regression to high-dimensional conditional density estimation.
- Izbicki, R., Shimizu, G., and Stern, R. B. (2022). Cd-split and hpd-split: Efficient conformal regions in high dimensions. *Journal of Machine Learning Research*, 23(87):1–32.
- Izbicki, R., Shimizu, G. T., and Stern, R. B. (2019). Flexible distribution-free conditional predictive bands using density estimators. *arXiv preprint arXiv:1910.05575*.
- Johnstone, C. and Cox, B. (2021). Conformal uncertainty sets for robust optimization. In *Conformal and Probabilistic Prediction and Applications*, pages 72–90. PMLR.
- Kivaranovic, D., Johnson, K. D., and Leeb, H. (2020). Adaptive, distribution-free prediction intervals for deep networks. In *International Conference on Artificial Intelligence and Statistics*, pages 4346–4356. PMLR.
- Krueger, D., Huang, C.-W., Islam, R., Turner, R., Lacoste, A., and Courville, A. (2017). Bayesian hypernetworks. *arXiv preprint arXiv:1710.04759*.
- Kuleshov, A., Bernstein, A., and Burnaev, E. (2018). Conformal prediction in manifold learning. In Gammerman, A., Vovk, V., Luo, Z., Smirnov, E., and Peeters, R., editors, *Proceedings of the Seventh Workshop on Conformal and Probabilistic Prediction and Applications*, volume 91 of *Proceedings of Machine Learning Research*, pages 234–253. PMLR.
- Lakshminarayanan, B., Pritzel, A., and Blundell, C. (2017). Simple and scalable predictive uncertainty estimation using deep ensembles. *Advances in neural information processing systems*, 30.
- Lei, J., G’Sell, M., Rinaldo, A., Tibshirani, R. J., and Wasserman, L. (2018). Distribution-free predictive inference for regression. *Journal of the American Statistical Association*, 113(523):1094–1111.
- Lei, J., Robins, J., and Wasserman, L. (2013). Distribution-free prediction sets. *Journal of the American Statistical Association*, 108(501):278–287.
- Lei, J. and Wasserman, L. (2014). Distribution-free prediction bands for non-parametric regression. *Journal of the Royal Statistical Society Series B: Statistical Methodology*, 76(1):71–96.
- McDermott, P. L. and Wikle, C. K. (2019). Deep echo state networks with uncertainty quantification for spatio-temporal forecasting. *Environmetrics*, 30(3):e2553.
- Meinshausen, N. (2006). Quantile regression forests. *Journal of Machine Learning Research*, 7(35):983–999.
- Messoudi, S., Destercke, S., and Rousseau, S. (2021). Copula-based conformal prediction for multi-target regression. *Pattern Recognition*, 120:108101.
- Messoudi, S., Destercke, S., and Rousseau, S. (2022). Ellipsoidal conformal inference for multi-target regression. In Johansson, U., Boström, H., An Nguyen, K., Luo, Z., and Carlsson, L., editors, *Proceedings of the Eleventh Symposium on Conformal and Probabilistic Prediction with Applications*, volume 179 of *Proceedings of Machine Learning Research*, pages 294–306. PMLR.
- Michelmore, R., Wicker, M., Laurenti, L., Cardelli, L., Gal, Y., and Kwiatkowska, M. (2020). Uncertainty quantification with statistical guarantees in end-to-end autonomous driving control. In *2020 IEEE International Conference on Robotics and Automation (ICRA)*, pages 7344–7350.
- Mobiny, A., Yuan, P., Moulik, S. K., Garg, N., Wu, C. C., and Van Nguyen, H. (2021). Dropconnect is effective in modeling uncertainty of bayesian deep networks. *Scientific reports*, 11(1):5458.
- Neeven, J. and Smirnov, E. (2018). Conformal stacked weather forecasting. In Gammerman, A., Vovk, V., Luo, Z., Smirnov, E., and Peeters, R., editors, *Proceedings of the Seventh Workshop on Conformal and Probabilistic Prediction and Applications*, volume 91 of *Proceedings of Machine Learning Research*, pages 220–233. PMLR.
- Papadopoulos, H., Proedrou, K., Vovk, V., and Gammerman, A. (2002). Inductive confidence machines for regression. In Elomaa, T., Mannila, H., and Toivonen, H., editors, *Machine Learning: ECML 2002*, pages 345–356, Berlin, Heidelberg. Springer Berlin Heidelberg.
- Papadopoulos, H., Vovk, V., and Gammerman, A. (2011). Regression conformal prediction with nearest neighbours. *Journal of Artificial Intelligence Research*, 40:815–840.
- Romano, Y., Patterson, E., and Candes, E. (2019). Conformalized quantile regression. In Wallach, H., Larochelle, H., Beygelzimer, A., d’Alché-Buc, F., Fox, E., and Garnett, R., editors, *Advances in Neural Information Processing Systems*, volume 32. Curran Associates, Inc.

- Rothfuss, J., Ferreira, F., Walther, S., and Ulrich, M. (2019). Conditional density estimation with neural networks: Best practices and benchmarks. *arXiv:1903.00954*.
- Seoni, S., Jahmunah, V., Salvi, M., Barua, P. D., Molinari, F., and Acharya, U. R. (2023). Application of uncertainty quantification to artificial intelligence in healthcare: A review of last decade (2013–2023). *Computers in Biology and Medicine*, 165:107441.
- Sesia, M. and Romano, Y. (2021). Conformal prediction using conditional histograms. *Advances in Neural Information Processing Systems*, 34:6304–6315.
- Shafer, G. and Vovk, V. (2008). A tutorial on conformal prediction. *Journal of Machine Learning Research*, 9(3).
- Singh, K. (2015). Facebook Comment Volume. UCI Machine Learning Repository. DOI: <https://doi.org/10.24432/C5Q886>.
- Stutz, D., Cemgil, A. T., Doucet, A., et al. (2021). Learning optimal conformal classifiers. *arXiv preprint arXiv:2110.09192*.
- Su, S., Li, Y., He, S., Han, S., Feng, C., Ding, C., and Miao, F. (2023). Uncertainty quantification of collaborative detection for self-driving. In *2023 IEEE International Conference on Robotics and Automation (ICRA)*, pages 5588–5594. IEEE.
- Sun, S. H. and Yu, R. (2024). Copula conformal prediction for multi-step time series prediction. In *The Twelfth International Conference on Learning Representations*.
- Taylor, J. W. (2000). A quantile regression neural network approach to estimating the conditional density of multiperiod returns. *Journal of forecasting*, 19(4):299–311.
- Tibshirani, R. J., Foygel Barber, R., Candès, E., and Ramdas, A. (2019). Conformal prediction under covariate shift. *Advances in neural information processing systems*, 32.
- Tumu, R., Cleaveland, M., Mangharam, R., Pappas, G., and Lindemann, L. (2024). Multi-modal conformal prediction regions by optimizing convex shape templates. In *Proceedings of the 6th Annual Learning for Dynamics & Control Conference*, volume 242 of *Proceedings of Machine Learning Research*, pages 1343–1356. PMLR.
- Valdenegro-Toro, M. (2019). Deep sub-ensembles for fast uncertainty estimation in image classification. *arXiv preprint arXiv:1910.08168*.
- Vovk, V., Gammerman, A., and Shafer, G. (2005). *Algorithmic learning in a random world*, volume 29. Springer.
- Wang, Z., Gao, R., Yin, M., Zhou, M., and Blei, D. (2023). Probabilistic conformal prediction using conditional random samples. volume 206 of *Proceedings of Machine Learning Research*, pages 8814–8836. PMLR.
- Wen, Y., Tran, D., and Ba, J. (2020). Batchensemble: an alternative approach to efficient ensemble and lifelong learning. In *International Conference on Learning Representations*.
- Xu, C., Jiang, H., and Xie, Y. (2024). Conformal prediction for multi-dimensional time series by ellipsoidal sets. In *Forty-first International Conference on Machine Learning*.

A Average m -Nearest Neighbor Distance

The average m -nearest neighbor distance for a generated sample $\hat{Y}_{i,k}$ can be computed as follows:

1. (Optional) Sample a sequence of reference samples $\{\tilde{Y}_{i,j}\}_{j=1}^M \sim \hat{p}(\cdot|X_i)$ for ranking estimation. Otherwise, set $\tilde{Y}_{i,l} = \hat{Y}_{i,l}$ for $l = 1, \dots, K$ and $M = K$.
2. Compute the pairwise distances of generated samples among reference samples:

$$D_i(k, l) := \|\hat{Y}_{i,k} - \tilde{Y}_{i,l}\|, \text{ for } k \in \{1, \dots, K\}, l \in \{1, \dots, M\}.$$

3. Sort the distances to $\hat{Y}_{i,k}$ such that:

$$D_i(k, (1)) \leq \dots \leq D_i(k, (M)),$$

where $D_i(k, (l))$ denotes the l -th smallest distance to $\hat{Y}_{i,k}$.

4. Calculate average m -nearest neighbor distance:

$$\bar{D}_{i,k} = \frac{1}{m} \sum_{l=1}^m D_i(k, (l)).$$

B Proof

B.1 Proof of Theorem 3.1

To prove the theorem, we first need to define the partial ordering between vectors, then we will define the empirical multivariate quantile function w.r.t. this partial ordering.

Definition B.1 (Vector partial order). We define a partial order \succ for K -dimensional vectors u, v as the following,

$$u \succ v \quad \text{i.f.f.} \quad \forall r \in \{1, \dots, K\}, u_r > v_r. \quad (9)$$

Proof. Based on the definition, we notice that

$$\mathbb{1}\{u \succ v\} = 1 - \max_{r=1, \dots, K} \mathbb{1}\{u_r \leq v_r\}.$$

We can rewrite the constraint in (6) as

$$\begin{aligned} \frac{1}{n+1} \sum_{i=\{1, \dots, n, \infty\}} \hat{S}_i(\beta) &= \frac{1}{n+1} \sum_{i=\{1, \dots, n, \infty\}} \max_{r=1, \dots, K} \mathbb{1}\{E_{i,r} \leq Q_r(\beta)\} \\ &= \frac{1}{n+1} \sum_{i=\{1, \dots, n, \infty\}} (1 - \mathbb{1}\{E_i \succ Q(\beta)\}) \\ &\geq 1 - \alpha, \end{aligned} \quad (10)$$

where for notation simplicity we let $Q(\beta) = (Q_1(\beta_1), \dots, Q_K(\beta_K))^\top$ denote the vector of quantiles and $E_i = (E_{i,1}, \dots, E_{i,r})^\top$ for $i = \{1, \dots, n, \infty\}$.

For a set of vectors $v_1, \dots, v_n \in \mathbb{R}^p$, we define the empirical multivariate quantile function as

$$\hat{Q}(\{v_1, \dots, v_n\}; 1 - \alpha) = \operatorname{argmin}_{\beta \in \mathbb{R}^K} \sum_{r=1}^K (Q_r(\beta_r))^d \quad (11)$$

$$\text{s.t.} \quad \frac{1}{n} \sum_{i=1}^n \mathbb{1}\{v_i \succ Q(\beta)\} \leq \alpha \quad (12)$$

We then observe that the minimizer β^* can be expressed with the defined empirical multivariate quantile function as

$$\beta^* = \hat{Q}(\{E_1, \dots, E_n\} \cup \{\infty\}, 1 - \alpha).$$

For a testing data (X_{n+1}, Y_{n+1}) and its non-conformity score vector E_{n+1} , from Lemma 1 in Tibshirani et al. (2019) we have the following equivalence,

$$E_{n+1} \succ \hat{Q}(\{E_1, \dots, E_n\} \cup \{\infty\}, 1 - \alpha) \iff E_{n+1} \succ \hat{Q}(\{E_1, \dots, E_n, E_{n+1}\}, 1 - \alpha). \quad (13)$$

By the exchangeability assumption and the equivalence, we have $\mathbb{P}(E_{n+1} \succ Q(\beta^*)) = \frac{\lfloor \alpha(n+1) \rfloor}{n+1} \leq \alpha$. We observe that its complement set achieves the target coverage, i.e.,

$$\mathbb{P}(\{E_{n+1} \succ Q(\beta^*)\}^c) = \mathbb{P}(\cup_{r=1}^K \{E_{n+1,r} \leq Q_r(\beta_r^*)\}) \geq 1 - \alpha.$$

By the definition of $\hat{C}_{\text{VCR}}(X_{n+1}; \beta)$, we have the following equivalence,

$$\cup_{r=1}^K \{E_{n+1,r} \leq Q_r(\beta_r^*)\} \iff Y_{n+1} \in \hat{C}_{\text{VCR}}(X_{n+1}; \beta^*).$$

Thus we prove that $\mathbb{P}(Y_{n+1} \in \hat{C}_{\text{VCR}}(X_{n+1}; \beta^*)) \geq 1 - \alpha$. □

B.2 Proof of Corollary 3.3

Proof. We first observe that for any $\hat{\beta}$ output by algorithm 2, it satisfies that

$$\frac{1}{n+1} \sum_{i=\{1, \dots, n, \infty\}} \hat{S}_i(\hat{\beta}) \geq 1 - \alpha,$$

which implies that $\sum_{i=\{1, \dots, n, \infty\}} \mathbb{1}\{E_i \succ Q(\hat{\beta})\} \leq \alpha$ by the derivation in equation (10). It implies that the rank of $Q(\hat{\beta})$ is of the top $\lfloor \alpha(n+1) \rfloor$ among $\{E_1, \dots, E_n, E_\infty\}$. By the exchangeability assumption and equation (13), $Q(\hat{\beta})$ is also of the top $\lfloor \alpha(n+1) \rfloor$ among $\{E_1, \dots, E_n, E_{n+1}\}$. We thus have $\mathbb{P}(E_{n+1} \succ Q(\hat{\beta})) = \frac{\lfloor \alpha(n+1) \rfloor}{n+1} \leq \alpha$ and its complement achieves the target coverage. The following steps are similar to the rest of the proof of Theorem 3.1.

Remark B.2. Note that any β satisfying the optimization constraint in (6) provides a valid coverage. In the multivariate case, there can exist a set of vectors that satisfy the constraint equation. Our proposed approximation algorithm searches within this set of valid vectors, ensuring that any output from the algorithm is valid. The distinction among these valid vectors lies in their corresponding efficiency, i.e., the objective function in (6). The minimizer β^* achieves the highest efficiency, and the approximated solutions progressively approach this minimizer through iterations, as demonstrated in Figure 2. □

C Efficient Algorithm for Quantile Optimization

Deriving β^* for small K and n can be done by grid search. However, grid search is no longer applicable even for $K \geq 5$. In this section, we propose an empirical method that computationally efficiently approximates β^* with linear complexity $\mathcal{O}(Kn)$ ($\mathcal{O}(K^2n)$ if apply the algorithm on all random sample positions).

The key idea of the approximation method is motivated by the “trade-off” between quantiles for different ranks. Intuitively, if one quantile is decreased then another quantile has to be increased to maintain coverage validity. During this trade-off, the efficiency changes accordingly. We present a simple demonstration of this idea for $K = 2$ in Figure 5. The colored region represents the feasible region in (6) with darker color indicating higher efficiency, and the red point shows the position of β^* . We can observe (i) a step-wise pattern on the boundary of the feasible region and (ii) β^* appears on the boundary. The step-wise pattern corresponds to the trade-off between β_1 and β_2 , which leads to different efficiency. Additionally, the feasible region is in a convex shape, also indicating the trade-off relationship between quantiles. Thus to approximate the optimal solution, we only need to find the boundary of the feasible region, and iteratively do the trade-offs between different quantiles.

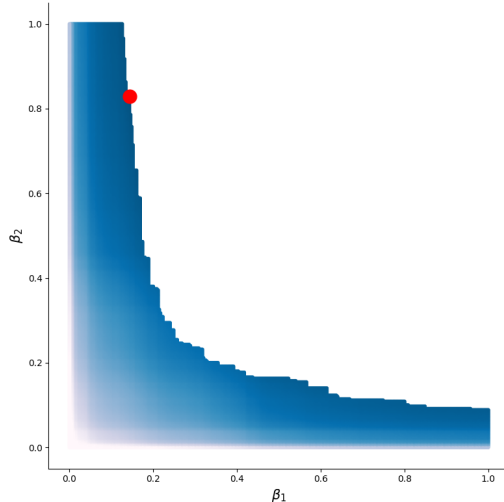


Figure 5: **Feasible region and optimal solution of optimization problem in (6) for $K = 2$.** The colored region shows the feasible region of β with darker color indicating higher efficiency and the red point shows the position of β^* .

To be more specific, the algorithm initializes a $\beta_k = 0$ and sets all the other entries of β to be 1. Then, we gradually increase β_k until the empirical coverage is just above the target coverage. The intuition behind such initialization is that it reduces the non-conformity score vector to the simple scalar case, as observed in the following equation,

$$\hat{S}_i(\beta) := \max_{r=1, \dots, K} \mathbb{1} \{E_{i,r} \leq Q_r(\beta_r)\} = \mathbb{1} \{E_{i,k} \leq Q_k(\beta_k)\}$$

for $\beta_k \neq 1$ and $\beta_j = 1$ for all $j \neq k$. Thus there exists such β_k that β can still satisfy empirical coverage with only $\beta_k \neq 1$. Let $\epsilon > 0$ denote a small increment, we then randomly pick another entry β_j for $j \neq k$ and do the trade-off between β_j and β_k . We set $\beta_k = \beta_k + \epsilon$, and decrease β_j until the empirical coverage is satisfied. Elementally, this process mimics the step-wise pattern, where we increase β_k and decrease β_j to do the trade-off and examine if the efficiency is improved. We iterate this process for different j until reach the budget. We show that empirically, the approximated solution $\hat{\beta}$ still achieves superior efficiency than baseline methods. We refer to Algorithm 2 for the complete details of the empirical approximation method. As a remark for practice, we set $\epsilon = 1/(n + 1)$ as default. But in cases, if the quantiles are not updated after several iterations, one may consider increasing ϵ for a larger trade-off.

D Implementation Details

For the estimation of conditional distribution for CQR and CHR, we implemented two base models, including quantile regression neural network (QNN) and quantile regression forest (QRF). We used QNN as the base model for CHR and CQR in the synthetic data experiments and QRF for the real data experiments. For the conditional probabilistic models for PCP and GCP-VCR, we conduct nearest neighbor regression (NN) for 1-dimensional synthetic data and mixture density network (MDN) for 2-dimensional synthetic data. For the real data experiments, we use QRF as the base models for PCP and GCP-VCR, the same with CHR and CQR.

- Quantile regression neural network (QNN). The network comprises three fully connected layers with ReLU activation functions. We used pinball loss to estimate the conditional quantiles for a grid of quantiles ranging from 0.01 to 1.0 with step size 0.01. The dropout rate is set to be 0.2. We train the model with 100 epochs using Adam optimizer with a learning rate equal to 0.001.
- Quantile regression forest (QRF). We set the minimum number of samples required to split an internal node to 50 and set the total number of trees to 100.
- Nearest neighbor regression (NN). We conduct NN with Python package *flexcode* and set the number of the nearest neighbor as 50 with a maximum of 31 basis functions.

Algorithm 2 Efficient Optimal Quantiles Search

1: **Input:** Non-conformity scores $\{E_i\}_{i=1}^n$; initial position k ; budget B ; increment ϵ .

2: **Initialize:**

$$\beta = \{\beta_1, \dots, \beta_K\} \leftarrow \underbrace{\{1, 1, \dots, 1\}}_{k-1}, \underbrace{\{0, 1, \dots, 1\}}_{K-k}.$$

3: **while** $\frac{1}{n+1} \sum_{i=\{1, \dots, n, \infty\}} \hat{S}_i(\beta) \geq 1 - \alpha + \frac{1}{n+1}$ **do**
4: $\beta_k \leftarrow \beta_k + \frac{1}{n+1}$;
5: **end while**
6: // Conducting trade-offs
7: **for** iter $\leftarrow 1$ to B **do**
8: sample $j \in \{1, \dots, K\}$ s.t. $j \neq k$;
9: $\beta'_k \leftarrow \beta_k + \epsilon$, $\beta'_j \leftarrow \beta_j$;
10: Set β'_k, β'_j as the k -th and j -th entry of β ;
11: **while** $\frac{1}{n+1} \sum_{i=\{1, \dots, n, \infty\}} \hat{S}_i(\beta) < 1 - \alpha$ **do**
12: $\beta'_j \leftarrow \beta'_j - \epsilon$;
13: **end while**
14: // Check if efficiency is improved
15: $r \leftarrow (Q_k(\beta_k))^d + (Q_j(\beta_j))^d$, $r' \leftarrow (Q_k(\beta'_k))^d + (Q_j(\beta'_j))^d$;
16: **if** $r > r'$ **then**
17: **continue**
18: **else**
19: Set β_k and β_j as the k -th and j -th entry of β ;
20: **end if**
21: **end for**
22: $\hat{\beta} \leftarrow \beta$;
23: **Output:** Approximated solution $\hat{\beta}$.

- Mixture density network (MDN). The implementation of MDN is conducted with Python package *cde*. We set the number of Gaussian mixture components as 10 and the hidden size as (100, 100). The other parameters are set to the default. We train the MDN model for 1,000 epochs with a dropout rate of 0.1.

E Experiments Results

In this section, we present the additional experimental results for synthetic data and MNIST data.

E.1 Synthetic Data Results

We present the visualizations of the prediction set provided by different baseline methods on S-shape, Circles, Spirals, Unbalanced clusters, and mixture-Gaussian data in Figure 6 and 7. For mixture-Gaussian data, we generate $X \sim \text{Uniform}(0, 1)$, and set $Y|X \sim 0.7N((X, 0)^T, I) + 0.3N((5 + X, 0)^T, I)$ for identity matrix $I \in \mathbb{R}^{2 \times 2}$. In the right subplot of Figure 7, we present the comparison of the prediction set of PCP and GCP-VCR. A key observation here is that in the low-density region (right component), GCP-VCR has a smaller radius for almost every circle, whereas in the high-density region (left component), GCP-VCR has a larger region covered. This demonstrates the ability of GCP-VCR to adapt to the local density by leveraging ranked samples.

Here, we also investigate the effect of K on coverage efficiency. We provide an example in Figure 8, which presents the ratio of PCP prediction set length over GCP-VCR prediction set length for S-shape data under different choices of $K = 3, 5, 10, 15, 20$ and different numbers of calibration data. The curve plot represents the mean, and the shaded area indicates the standard error of the ratio over 100 experiments. Under all settings, the ratio consistently remains above 1, showing that GCP-VCR provides a more efficient prediction set. Additionally, the ratio decreases as K increases, suggesting that the benefit of GCP-VCR decreases with larger K .

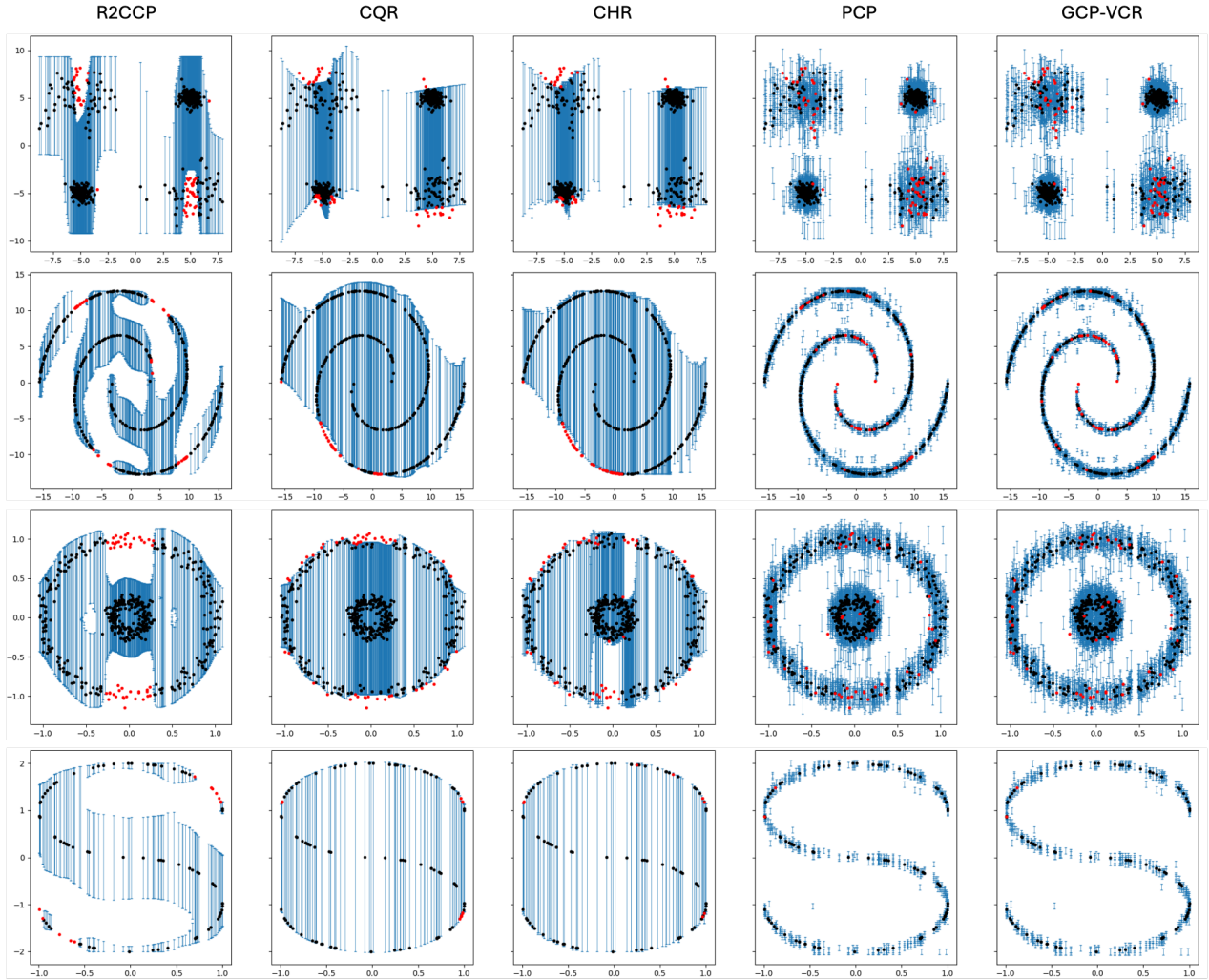


Figure 6: Comparison of prediction set ($\alpha = 0.1$) generated by different methods on 1-dimensional synthetic data: S-shape, Circles, Spirals, and Unbalanced clusters (from top to bottom row). Blues lines: the predictive intervals of each method; Black dots: test points that are covered by the predictive sets; Reds dots: test points not covered. We plot the figure with 100, 500, 400, and 500 random samples for each data, respectively.

E.2 MNIST Data Results

In Figure 9, we present the mean and standard error of the miscoverage rate of PCP and GCP-VCR for MNIST experiment with different K . The blue and red bars indicate the miscoverage rate of PCP and GCP-VCR, respectively. The dark line shows the standard error of miscoverage rate over 30 experiments. We observe that GCP-VCR consistently provides a lower miscoverage rate than PCP, indicating a higher efficiency of the prediction set. This also explains why the random images of GCP-VCR aligns more closely with the target as shown in Figure 3.

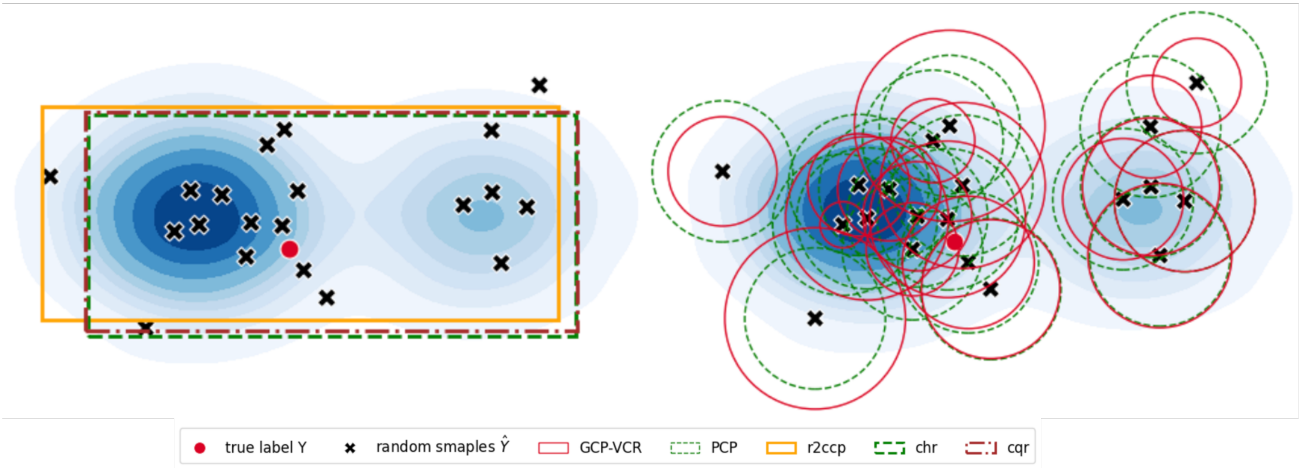


Figure 7: Comparison of prediction set ($\alpha = 0.1$) generated by different methods on 2-dimensional synthetic mixture Gaussian data. The mixture Gaussian data is generated with 2 components with weights 0.7 and 0.3 from left to right, respectively. The blue shade indicates the true conditional density. In the left subplot, we present the rectangle-shaped prediction regions generated by CQR, CHR and R2CCP. In the right subplot, we present the circle-shaped prediction regions provided by GCP-VCR and PCP.

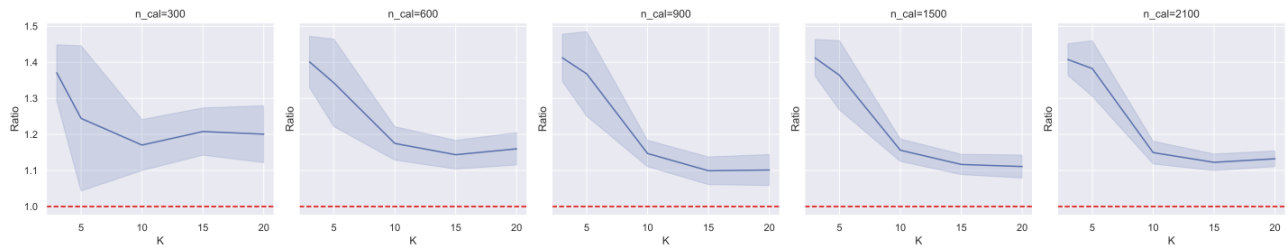


Figure 8: Ratio of PCP prediction set length over GCP-VCR prediction set length under different $K = 3, 5, 10, 15, 20$ and number of calibration data for S-shape data. The blue curve represents the mean, and the shaded area indicates the standard error of the ratio. We observe that the ratio remains consistently above 1, demonstrating that GCP-VCR achieves better efficiency.

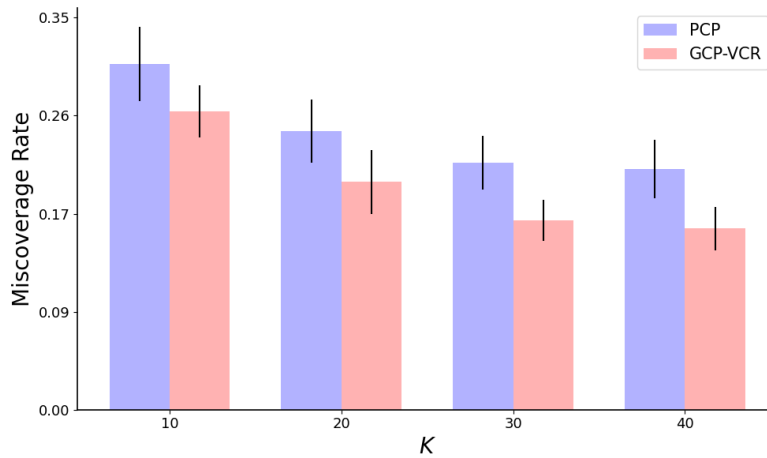


Figure 9: Comparison of miscoverage rate of PCP and GCP-VCR for MNIST data under different K . The blue and red bars represent PCP and GCP-VCR results, respectively, with black lines showing the standard error of the miscoverage rate across 30 experiments. GCP-VCR consistently achieves a lower miscoverage rate than PCP, indicating a more efficient prediction set.